Chemical Science

EDGE ARTICLE

Light-induced electronic structure modulation in perovskite ferrite for efficient photothermal dry reforming of methane

Jilong Li, [ab] Xiang Hao, [ab] Jiwu Zhao, [ab] Jinyu Li, [c] Bo Su, [ab] Zhengxin Ding, *[ab] Meirong Huang, [ab] Zhi-An Lan, [ab] Min-Quan Yang *[c] and Sibo Wang *[ab]

Solar-driven dry reforming of methane (DRM) offers a sustainable pathway to convert CH_4 and CO_2 into valuable syngas feedstock, yet the efficiency is hindered by the sluggish lattice oxygen (LO) migration of the catalyst and the incomplete understanding of light-enhanced redox cycling. Here, we demonstrate that $Ru/LaFeO_3$ functions as a highly efficient and durable photothermal catalyst for DRM. The incorporation of Ru not only serves as an electron trap but also modulates the catalyst's electronic structure. Notably, under light irradiation, photoinduced charge redistribution further intensifies this electronic modulation, leading to electron enrichment at Ru, La, and Fe sites, and hole accumulation at LO sites. This interfacial charge dynamics weakens La−O and Fe−O bonds and facilitates LO migration, enabling efficient CH_4 activation and oxidation at Ru sites, accompanied by the generation of oxygen vacancies (OVs). Simultaneously, the *in situ* generated OVs promote CO_2 adsorption and activation, facilitating its cleavage into CO and replenishing the OVs, thereby sustaining the redox cycle for continuous catalysis. This study provides key mechanistic insights into photoinduced LO dynamics driven by charge redistribution, and offers valuable guidance for the rational design of advanced photothermal systems that leverage both thermal and photonic effects of solar energy for enhanced catalysis *via* the LO-mediated pathways.

Introduction

Dry reforming of methane (DRM) ($CH_4 + CO_2 \rightarrow 2CO + 2H_2$, $\Delta H_{298K} = 247$ kJ mol^{-1}) offers a promising route for converting two major greenhouse gases into syngas, a valuable feedstock for various chemical process.[1–4] However, due to the high bond dissociation energies of the C–H bond (434 kJ mol^{-1}) in CH_4 and the C=O bond (805 kJ mol^{-1}) in CO_2,[5–10] conventional thermal catalytic DRM typically proceeds at elevated temperatures of 700–1000 °C, which is highly energy-intensive and carbon emissive.[11] Moreover, harsh conditions often lead to undesirable side reactions such as CH_4 decomposition and CO disproportionation, resulting in carbon deposition, catalyst sintering, and deactivation.[12,13]

To overcome these limitations, solar-driven DRM has emerged as a sustainable and potentially low-temperature

alternative.[14–20] This approach is generally understood to follow a light-enhanced Mars–van Krevelen (MvK) mechanism in metal oxide catalysts.[15,20–23] The key reaction process typically involves CH_4 splitting into CH_x^* ($0 \leq x \leq 3$) and H* species, and lattice oxygen (LO) migration to react with CH_x^*, ultimately forming CO and suppressing coke formation.[14,15,18] However, strong metal–oxygen interactions in normal metal oxides significantly limit LO mobility, restricting overall catalytic activity.[24] In addition, the chemical inertness of the reactants and the multistep nature of DRM introduce further challenges in achieving efficient activation of both the C–H and C=O bonds under mild conditions while controlling reaction pathways.[25,26]

Perovskite oxides (ABO_3) have recently garnered increasing attention as promising platforms for photothermal DRM catalysis.[14–16,18,20,21] These materials feature corner-sharing BO_6 octahedra formed by A-site (typically rare-earth) and B-site (transition metal) ions, offering enhanced light absorption and efficient charge separation.[27–32] Their compositional tunability and intrinsic LO activity enable dynamic modulation of catalytic properties.[20,33] Indeed, several studies have confirmed the feasibility of light-driven DRM over perovskite-based systems.[14–16,21,34] Nonetheless, developing photothermal catalysts with high efficiency and long-term stability remains a critical goal. Moreover, unlike conventional thermal catalysis that occurs in the electronic ground state, photothermal DRM operates under

[a]State Key Laboratory of Chemistry for NBC Hazards Protection, College of Chemistry, Fuzhou University, Fuzhou 350116, China

[b]State Key Laboratory of Photocatalysis on Energy and Environment, College of Chemistry, Fuzhou University, Fuzhou 350116, P. R. China. E-mail: zxding@fzu.edu.cn; sibowang@fzu.edu.cn

[c]College of Environmental and Resource Sciences, College of Carbon Neutral Modern Industry, Fujian Normal University, Fuzhou, 350117, P. R. China. E-mail: yangmq@fjnu.edu.cn

photoexcited states, in which the electronic structure of the catalyst is continuously modulated by photoexcited charge carriers.[15,18,20] Yet, the fundamental understanding of how these photoinduced carriers influence catalytic performance remains incomplete and warrants further investigation.

Herein, we present a novel photothermal catalyst composed of Ru NPs supported on $LaFeO_3$, which manifests excellent DRM activity and durability. Under a light intensity of 6.7 W cm^{-2}, the catalyst delivers CO and H_2 production rates of 34.14 and 27.92 mol g_{Ru}^{-1} h^{-1}, respectively, with an outstanding CH_4 turnover frequency (TOF_{CH_4}) of 0.64 s^{-1} and an excellent light-to-chemical energy efficiency (LTCEE) of 16.3%. Combined experimental and theoretical studies reveal that strong interfacial interaction between Ru and $LaFeO_3$ enhances electron distribution at La and Fe sites, while light irradiation further strengthens such an effect. The charge redistribution of Ru/$LaFeO_3$ results in electron enrichment on Ru, La and Fe sites, while holes are accumulated on LOs. The synergistic electronic modulation weakens La/Fe–O bonds and facilitates LO migration, enabling rapid LO-involved CH_4 activation and oxidation at Ru sites, accompanied by the formation of oxygen vacancies (OVs). Concurrently, the *in situ* generated OVs efficiently adsorb and activate CO_2, promoting its cleavage into CO, coupled with O to refill OVs, completing the catalytic cycle.

Results and discussion

The $LaFeO_3$ perovskite catalyst was synthesized *via* a sol–gel method, followed by calcination to enhance the crystallinity.[28] Fig. S1 displays the powder X-ray diffraction (XRD) pattern of $LaFeO_3$, which matches well with the standard card of the

orthorhombic structure (JCPDS no. 37-1493).[28] Transmission electron microscopy (TEM) shows an irregular nanoparticle morphology for $LaFeO_3$ (Fig. S2a). The high-resolution TEM (HRTEM) image presents clear lattice fringes with a d-spacing of 0.28 nm (Fig. S2b) that corresponds to the (121) plane, confirming the high crystallinity of the synthesized $LaFeO_3$.[27] Subsequently, Ru nanoparticles (NPs) were deposited onto the $LaFeO_3$ surface by an impregnation–reduction method. Energy dispersive spectroscopy (EDS) analysis confirms the successful loading of Ru NPs (Fig. S3). Inductively coupled plasma optical emission spectrometry (ICP-OES) reveals that the actual contents of Ru loading closely match the theoretical values (Table S1). Notably, the catalyst used in all subsequent experiments is the 1.0% Ru/$LaFeO_3$ sample unless otherwise stated, which is referred to as Ru/$LaFeO_3$ for brevity.

TEM analysis of the Ru/$LaFeO_3$ catalyst reveals that the introduction of Ru has minimal impact on the morphology of $LaFeO_3$ (Fig. S4). The Ru species are dispersed as ultra-small nanoparticles with an average size of 2.3 nm on the surface of $LaFeO_3$ (Fig. 1 and S5). In the HRTEM image (Fig. 1b), two sets of lattice fringes with d-spacings of 0.21 and 0.28 nm are observed, corresponding to the (101) plane of Ru NPs and (121) plane of $LaFeO_3$, respectively. The EDS elemental mapping of Ru/$LaFeO_3$ shows that Ru, La, Fe, and O are homogeneously distributed across the individual particles (Fig. 1c), suggesting a high degree of Ru dispersion. Moreover, the XRD pattern of Ru/$LaFeO_3$ closely resembles that of pristine $LaFeO_3$. No noticeable diffraction peaks attributable to Ru species are detected, further confirming the high dispersion and ultra-small nature of the loaded Ru NPs (Fig. 1d and S5).

X-ray photoelectron spectroscopy (XPS) was applied to check the chemical states of elements in the samples (Fig. S6). The Ru
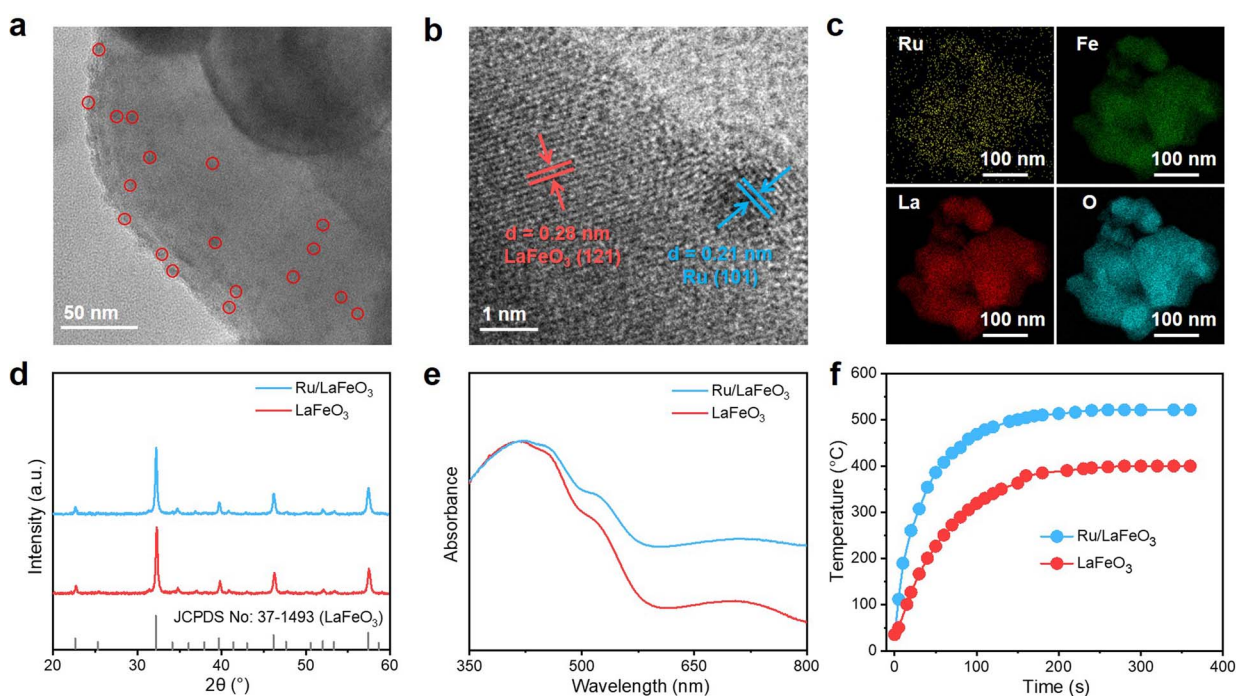

Fig. 1 (a) TEM image, (b) HRTEM image and (c) EDS elemental maps of Ru/$LaFeO_3$. (d) XRD patterns and (e) DRS of $LaFeO_3$ and Ru/$LaFeO_3$ catalysts. (f) Surface local temperature evolution of $LaFeO_3$ and Ru/$LaFeO_3$ catalysts under 6.7 W cm^{-2} light irradiation.

3p spectrum of Ru/LaFeO$_3$ reveals that Ru species are mainly present as metallic Ru^0 (462.8 and 484.9 eV), along with a minor portion of Ru^{4+} (465.3 and 487.4 eV) (Fig. S6a).[28] In the Fe 2p region (Fig. S6b), the peaks at 711.1 and 724.5 eV correspond to Fe^{3+}, whereas those at 709.6 and 723.1 eV are assigned to Fe^{2+}.[29] The La 3d spectra exhibit characteristic doublets (Fig. S6c), which can be deconvoluted into La 3d$_{5/2}$ (833.59, 835.70, 837.72, and 838.75 eV) and La 3d$_{3/2}$ (850.42, 851.90, 854.55, and 855.59 eV). In the La 3d$_{5/2}$ region, the spectrum can be deconvoluted into two distinct doublets. The first doublet corresponds to the lattice La–O species in the perovskite framework, with the main peak at 833.59 eV and a satellite at 837.72 eV. The second doublet arises from La(OH)$_3$, featuring a main peak at 835.70 eV and its associated satellite at 838.75 eV.[15] The O 1s spectrum consists of two components at 529.3 and 531.4 eV (Fig. S6d), assigned to LO and adsorbed oxygen (AO), respectively. The relative intensity of the AO component is generally correlated with the density of surface OV, providing valuable information on the defect chemistry of the catalyst.

Notably, XPS reveals strong electronic interactions between Ru NPs and LaFeO$_3$, which change the electron density of LaFeO$_3$. After Ru loading, the Fe species in Ru/LaFeO$_3$ exhibit a more electron-rich state compared to those in bare LaFeO$_3$.[15] Meanwhile, the surface La–OH species undergo a dehydration process to form La–O bonds, accompanied by the generation of OVs, as evidenced by changes in the O 1s spectrum. The formation of these oxygen vacancies facilitates the activation of the C=O bond in CO$_2$ and thus promotes the DRM reaction.[35,36]

The light harvesting properties of the catalysts have been investigated using UV-Vis diffuse reflectance spectroscopy (DRS). Pristine LaFeO$_3$ exhibits an intrinsic interband transition below 550 nm, with a bandgap energy of 2.12 eV as determined from the Tauc plot (Fig. S7a). The Mott–Schottky curves indicate that the conduction band (CB) edge of LaFeO$_3$ is positioned at −0.83 V (vs. NHE) (Fig. S7b). Combined with the optical band gap, the valence band (VB) edge is estimated to be 1.29 V (Fig. S7c). Compared with bare LaFeO$_3$, Ru loading greatly enhances light absorption across a broad spectral range from the ultraviolet to the visible-near-IR region (200–800 nm), endowing Ru/LaFeO$_3$ with excellent "nano-heater" functionality (Fig. 1e).

Comparison of the VB potentials of Ru/LaFeO$_3$ and LaFeO$_3$ indicates that Ru incorporation noticeably modulates the electronic structure of LaFeO$_3$ (Fig. S7d–f), which strengthens its oxidation capability. This modulation is further corroborated by the distinct binding energy shifts observed in the O 2p region of the VB XPS spectra (Fig. S8). On this basis, the photothermal conversion performances of the catalysts were evaluated under same light intensities using a thermocouple placed in close contact with the catalyst surface. At a light intensity of 6.7 W cm^{-2}, the surface temperature of the Ru/LaFeO$_3$ catalyst reaches 520 °C, which is much higher than that of bare LaFeO$_3$ (Fig. 1f). The results highlight the strong potential of using Ru/LaFeO$_3$ as an efficient light harvesting platform to drive DRM under relatively mild conditions.

Using a fixed-bed continuous flow system without external heating, the light-driven DRM performance of the catalysts was evaluated. As shown in Fig. S9, the optimal Ru loading is determined to be 1%, at which the Ru/LaFeO$_3$ sample shows the best catalytic performance. The production rates of CO and H$_2$ reach 34.14 and 27.92 mol g$_{Ru}^{-1}$ h^{-1}, respectively, which are comparable or better than those of state-of-the-art catalysts.[14–18,21,25,37] Isotope labelling experiments confirm that the generated CO comes from the conversion of CH$_4$ and CO$_2$ (Fig. S10). Notably, pristine LaFeO$_3$ exhibits no activity under light irradiation (Fig. 2a), indicating the essential role of Ru species in this catalytic process. For comparison, the catalytic performances of Ru/Fe$_2$O$_3$ and Ru/La$_2$O$_3$ were also tested (Fig. 2a), which exhibit markedly weakened performance compared to Ru/LaFeO$_3$. These results highlight that the perovskite structure of LaFeO$_3$ plays a critical role in enabling high activity for photothermal DRM.[15,31]

Moreover, the thermocatalytic DRM performance of the Ru/LaFeO$_3$ catalyst driven by external heating under equivalent temperature as that of photothermal conditions was also evaluated. Compared to the thermal catalytic process (Fig. 2b), H$_2$ and CO production of Ru/LaFeO$_3$ under photothermal conditions increased by about 2.4 and 1.7 times, respectively. In particular, in the temperature range of 350–550 °C, the efficiencies of photothermal DRM consistently outperform those of thermocatalysis (Fig. S11). At a catalyst surface temperature of 550 °C, CH$_4$ conversion reaches 38.7%, corresponding to a TOF$_{CH_4}$ 0.64 s^{-1},[2] denoting excellent CH$_4$ conversion capability. Importantly, the CH$_4$ conversions of light-driven DRM significantly exceed the thermal equilibrium limits within the examined temperature range (Fig. 2c). This implies that the light-driven process integrates thermocatalytic and photocatalytic processes, that is, involving solar heating and photoexcitation.[19,38,39] Under a constant light intensity of 6.7 W cm^{-2} by adjusting the distance between the light source and the catalyst, narrowing the light spectrum leads to a gradual decline in the catalytic activity of Ru/LaFeO$_3$ (Fig. S12). Nevertheless, the photothermal DRM efficiencies remain much higher than those achieved under purely thermal conditions, confirming the essential contribution of photoexcited charges in promoting the reaction.

In the DRM process, the water–gas conversion reaction is an unavoidable reverse reaction, which generally results in a low ratio of H$_2$/CO.[19,40] However, under light-driven photothermal conditions, the H$_2$/CO ratios are significantly improved compared to those under thermal-driven process (Fig. 2d). The finding highlights the key role of the light-induced effects in regulating the reaction pathway. LTCEEs measured under different light intensities reveal that the Ru/LaFeO$_3$ catalyst exhibits increased LTCEEs with enhancing light intensity, reaching an impressive 16.3% at 7.2 W cm^{-2} (Fig. 2e), which is higher than the latest reported value.[15,18,20] Furthermore, the Arrhenius plot analysis reveals that the apparent activation energy (E$_a$) for thermal catalysis (84.0 kJ mol^{-1}) on the Ru/LaFeO$_3$ catalyst is much higher than that for photothermal DRM (59.1 kJ mol^{-1}) (Fig. 2f), indicating that light irradiation alters the reaction pathway, thereby lowering the apparent reaction energy barrier.[33] Finally, the durability test of the Ru/LaFeO$_3$ catalyst reveals outstanding stability, which retains
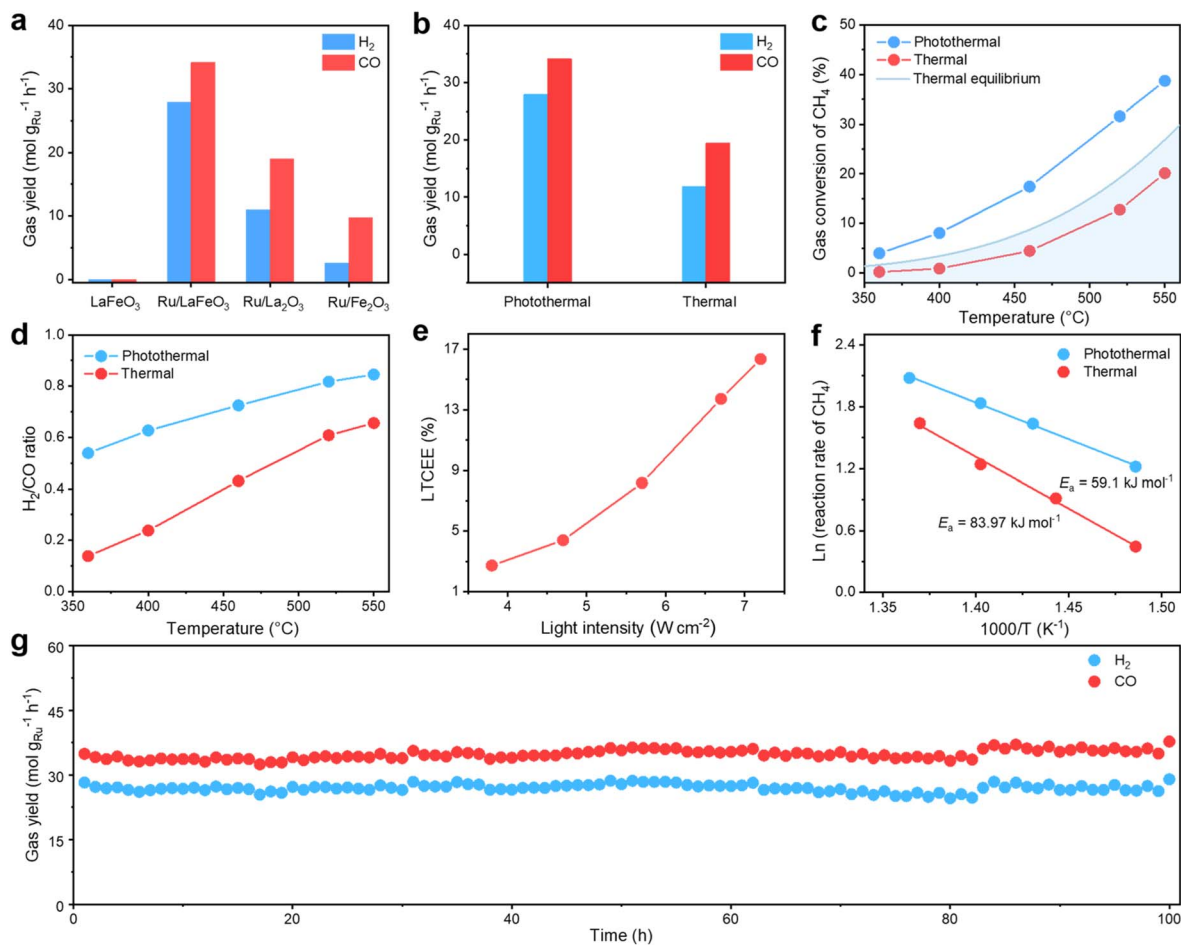
Fig. 2 (a) DRM performances of different catalysts under light-driven conditions (catalyst: 80 mg; light intensity: 6.7 W cm^{-2}; feedstocks: CO$_2$/CH$_4$/He = 47/47/6, GHSV = 22.5 L g^{-1} h^{-1}). (b) DRM activities of Ru/LaFeO$_3$ under photothermal and thermal conditions. (c) CH$_4$ conversion under photothermal and thermal conditions at different temperatures. (d) H$_2$/CO ratios of DRM at different temperatures powered by pure light irradiation and external heating. (e) LTCEEs of Ru/LaFeO$_3$ under different incident intensities. (f) Arrhenius plots of CH$_4$ in photothermocatalysis and thermocatalysis by Ru/LaFeO$_3$. (g) Stability test of Ru/LaFeO$_3$ in light-driven DRM.

stable photothermal DRM activity over 100 h, delivering a turnover number of 3.54×10^5 calculated by the H$_2$ production.[2] XPS analysis reveals an increased proportion of lower-valent Ru and Fe species in Ru/LaFeO$_3$ after the reaction (Fig. S13 and S14). This can be ascribed to the strongly reducing atmosphere, which drives the metal sites toward lower oxidation states.[19,36] However, the XRD pattern of the post-reaction Ru/LaFeO$_3$ catalyst shows no detectable structural changes (Fig. S15). Together with the stability tests, these results suggest that the reduction process does not compromise the catalyst's performance significantly, which may point to the involvement of reversible structural dynamics. In sharp contrast, XRD analysis shows that Ru/Fe$_2$O$_3$ is transformed into Ru/Fe$_3$O$_4$ after only 10 min of reaction (Fig. S16). These results further verify that the perovskite structure of LaFeO$_3$ ensures both high activity and robust stability in photothermal DRM.[15,31]

To investigate the origin of the high performance of Ru/LaFeO$_3$ in the light-driven DRM reaction, temperature-programmed desorption (TPD) tests were conducted to assess the interactions between reactant molecules (CH$_4$ and CO$_2$) and

the catalysts. In the CH$_4$-TPD profiles (Fig. S17), the desorption peaks of Ru/LaFeO$_3$ appeared at higher temperatures and with stronger intensities compared with those of bare LaFeO$_3$, suggesting that the loading of Ru provides stronger active sites and promotes the chemisorption and activation of CH$_4$.[15] In contrast, the CO$_2$-TPD results show that upon Ru loading, the physical adsorption of CO$_2$ becomes weaker while chemisorption is significantly enhanced (Fig. 3a).[17,41] This can be attributed to the electron transfer from loaded Ru NPs to LaFeO$_3$ (as evidenced by XPS analysis), which increases the surface electron density and strengthens the CO$_2$-catalyst interactions, thus shifting CO$_2$ adsorption from physisorption to chemisorption.[35,36] The chemisorbed CO$_2$ is more likely to participate in the subsequent catalytic reactions. Fig. 3b shows the linear scanning voltammetry (LSV) measurement, which shows an increase in current density and a decrease in onset potential for Ru/LaFeO$_3$, providing further evidence of its enhanced CO$_2$ activation capacity.[42]

Moreover, the separation and migration kinetics of photo-induced carriers were systematically investigated using
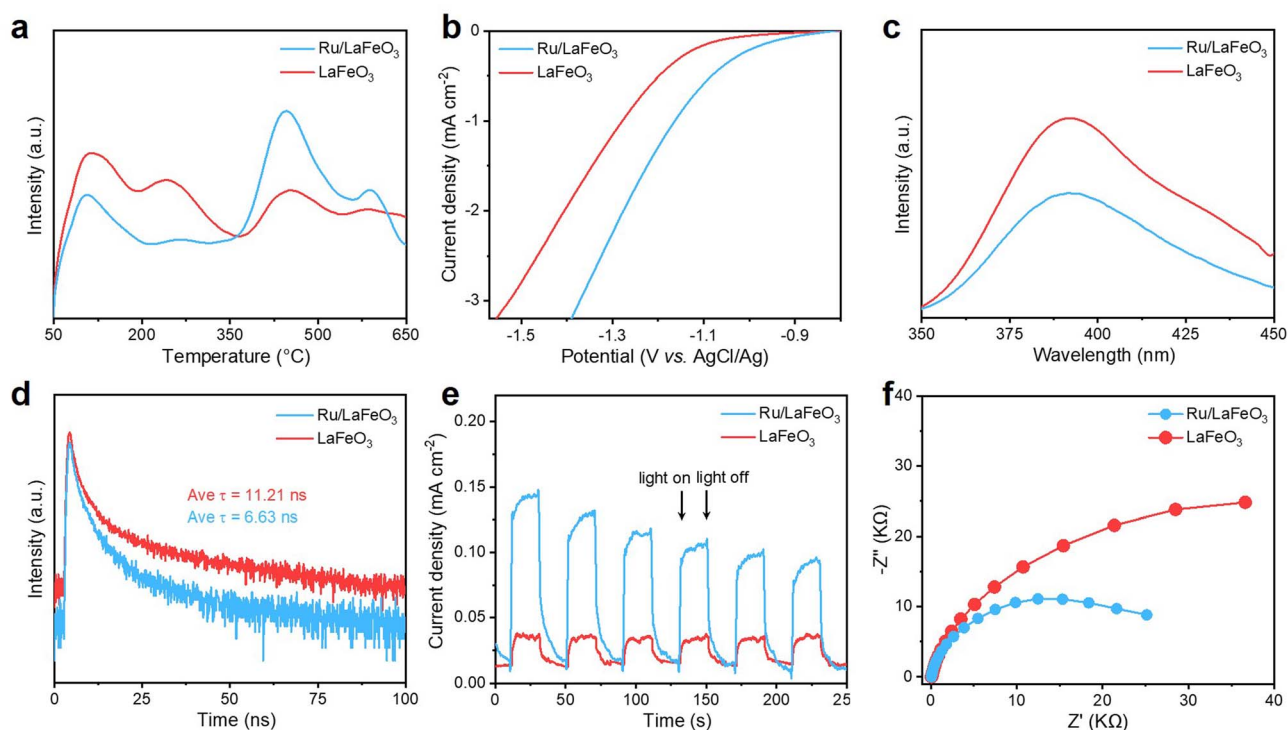
Fig. 3 (a) CO_2-TPD, (b) LSV curves, (c) steady-state PL spectra, (d) TRPL spectra, (e) transient photocurrent responses, and (f) EIS Nyquist plots of $LaFeO_3$ and $Ru/LaFeO_3$.

photoluminescence (PL) and electrochemical techniques. Steady-state PL and time-resolved PL (TRPL) analyses indicate that $Ru/LaFeO_3$ effectively inhibits the recombination of charge carriers and promotes their separation compared to bare $LaFeO_3$ (Fig. 3c and d).[43–47] In addition, the photocurrent response of $Ru/LaFeO_3$ is markedly higher than that of $LaFeO_3$ (Fig. 3e), which is consistent with the electrochemical impedance spectroscopy (EIS) results showing a lower charge-transfer resistance of $Ru/LaFeO_3$ (Fig. 3f).[48–52] These findings collectively verify that Ru modification facilitates the separation and utilization of photoinduced charges, thereby contributing to enhancing the DRM activity under light irradiation.

To further identify the active sites in $Ru/LaFeO_3$ for CH_4 and CO_2 conversion, light-driven control experiments were conducted under pure CH_4 and CO_2 atmospheres, respectively.[20] The results show that CO and H_2 are detected on $Ru/LaFeO_3$ in a CH_4 atmosphere, whereas no products are observed on bare $LaFeO_3$ (Fig. S18). Moreover, no detectable products generate on $LaFeO_3$ under a pure CO_2 atmosphere, regardless of the presence or absence of Ru species (Fig. S19). These findings indicate that Ru NPs serve as the active sites for CH_4 dissociation. Notably, during the reaction under pure CH_4, CO production on $Ru/LaFeO_3$ rapidly ceases, while the production of H_2 gradually decreases (Fig. S20). Meanwhile, the electron paramagnetic resonance (EPR) analysis of $Ru/LaFeO_3$ after reaction in pure CH_4 shows an obviously enhanced OV signal (Fig. S21). This phenomenon can be attributed to the oxidation of CH_4 by surface-active LOs; as LOs become depleted, deep dehydrogenation of CH_4 leads to carbon deposition that blocks the active

site (Fig. S22). Furthermore, when the deactivated $Ru/LaFeO_3$ catalyst (which, after reaction in CH_4, is subsequently exposed to pure CO_2 under light radiation), CO generation is clearly detected (Fig. S23). Correspondingly, the EPR analysis shows diminished OVs signal on the $Ru/LaFeO_3$, indicating the replenishment of oxygen atoms into the vacancies (Fig. S21). These observations, combined with the absence of CO production over $LaFeO_3$ under identical conditions, indicate that the OVs generated in $LaFeO_3$ serve as the active centers for CO_2 reduction to CO. This mechanism is further supported by the ^{18}O-labelling experiments, which confirm the involvement of LOs in photothermal DRM (Fig. S24). In brief, the LOs in $Ru/LaFeO_3$ facilitate the oxidation of CH_4 to generate CO and H_2, while simultaneously creating OVs. These vacancies then dissociate CO_2 to produce CO and replenish O atoms, thus regenerating the LOs.[14,20,53]

To gain deeper insight into the photothermal catalytic mechanism of DRM over $Ru/LaFeO_3$, a series of in situ characterization experiments and theoretical calculations were performed. Under light irradiation, the in situ XPS (ISI-XPS) measurement for the $Ru/LaFeO_3$ catalyst exhibits negative shifts in the binding energies of Ru 3p, Fe 2p, and La 3d, along with a positive shift in O 1s. These shifts indicate the accumulation of photoexcited electrons on the metal sites of Ru, Fe, and La, and the localization of photogenerated holes on LOs (Fig. 4a–c and S25).[15,20] Under the reducing influence of photogenerated electrons, the catalyst undergoes electronic rearrangement, leading to a shift of Ru and Fe species toward lower oxidation states (Fig. S26). Meanwhile, the decreased proportion of La–
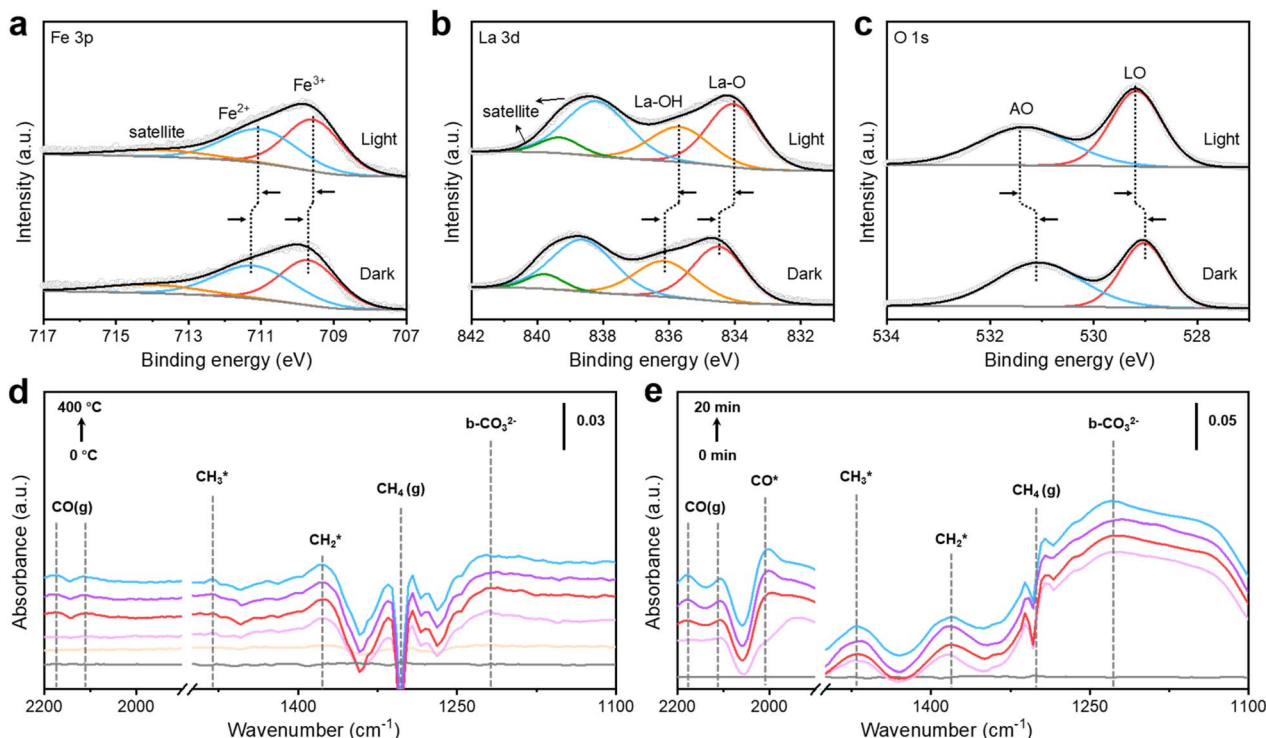
Fig. 4 ISI-XPS spectra of (a) Fe 2p, (b) La 3d and (c) O 1s of Ru/LaFeO₃. (d and e) *In situ* DRIFTS spectra of Ru/LaFeO₃ catalysts in CO₂/CH₄-saturated atmosphere under (d) external heating and (e) light irradiation.

OH can be ascribed to light-induced desorption of surface-adsorbed species, a phenomenon that is also reflected in the O 1s spectrum. This light-induced electronic restructuring in the catalyst is pivotal for enhancing both the efficiency and stability of the DRM reaction, as discussed below. The photoexcited electrons captured at the Ru site facilitate the H* to H₂ transition. Simultaneously, electron accumulation on Fe and La species enhances their electron densities, weakening their bonding with oxygen atoms and promoting the mobility of LOs.[18] The hole accumulation on the LOs enhances their oxidative reactivity, thereby improving CH₄ conversion.[54] Additionally, the elevated electron densities at Fe and La sites reduce the reactive energy barriers for CO₂ molecules trapped by OVs, thus promoting both CO₂ activation and the regeneration of LOs.[35,36]

To track the key reaction intermediates, *in situ* DRIFTS was performed on the catalysts in a DRM atmosphere. The DRIFTS spectra of Ru/LaFeO₃ recorded in the dark show effective adsorption of CO₂ (2300–2400 cm⁻¹) and CH₄ (3016 and 1242–1350 cm⁻¹) (Fig. S27).[55–58] After reaching adsorption equilibrium, the IR spectrum was recorded as a baseline. Upon heating, inverted peaks of CO₂ and CH₄ emerged under thermal-driven conditions (Fig. S28), indicating the consumption of adsorbed CH₄ and CO₂ molecules. Meanwhile, signals ascribed to bidentate carbonate (b-CO₃²⁻, 1230 cm⁻¹)[17] and CO (2112 and 2184 cm⁻¹) appear,[59] indicating CO₂ activation and CO formation (Fig. 4d). In addition, the appearance of the CH₃* signal (1480 cm⁻¹) can be attributed to the dehydrogenation of adsorbed CH₄.[60] Under photothermal conditions, the DRIFTS

spectra of the Ru/LaFeO₃ catalyst are significantly different. The signals for b-CO₃²⁻, CO(g), and CH₃* are gradually enhanced with continuous light irradiation (Fig. 4e). Meanwhile, a distinct signal of CH₂* at 1370 cm⁻¹ appears,[17] indicating further dehydrogenation of CH₃*. This intermediate is subsequently converted to CO and H₂ through additional dehydrogenation steps. These findings suggest that light irradiation significantly boosts activation and dissociation of CH₄ and CO₂, aligning well with the improved photothermal DRM activity.

Finally, DFT calculations were performed to theoretically validate the activation and transformation processes of CH₄ and CO₂ on Ru/LaFeO₃ (Fig. 5). Initially, CH₄ adsorbs onto the Ru site with an adsorption energy of 0.7 eV (step I). Subsequently, the C–H bond undergoes cleavage, yielding CH₃* and H* species (step II). After that, a deep dehydrogenation of CH₃* proceeds, leading to the formation of C* and the stepwise release of all H* (steps III–VI), forming two H₂ molecules at the Ru site (steps IV–VII). Concurrently, migration of LO on the Ru/LaFeO₃ surface proceeds to generate reactive O* and OV (steps IX–XI). This oxygen transfer process encounters the highest energy barrier of 1.47 eV in the transition state (TS), identifying it as the rate-determining step. The migrated O* then reacts with C* to form CO*. Meanwhile, the generated OV facilitates the adsorption of CO₂ with an adsorption energy of −0.76 eV (step XII). After adsorption, CO₂ dissociates with an energy barrier of −0.29 eV to produce CO* (step XIII) and releases O atoms that replenish the OVs. Finally, CO* desorbs from the catalyst surface, completing the CO generation process (steps XIV and XV). These results highlight the high effectiveness of Ru/LaFeO₃
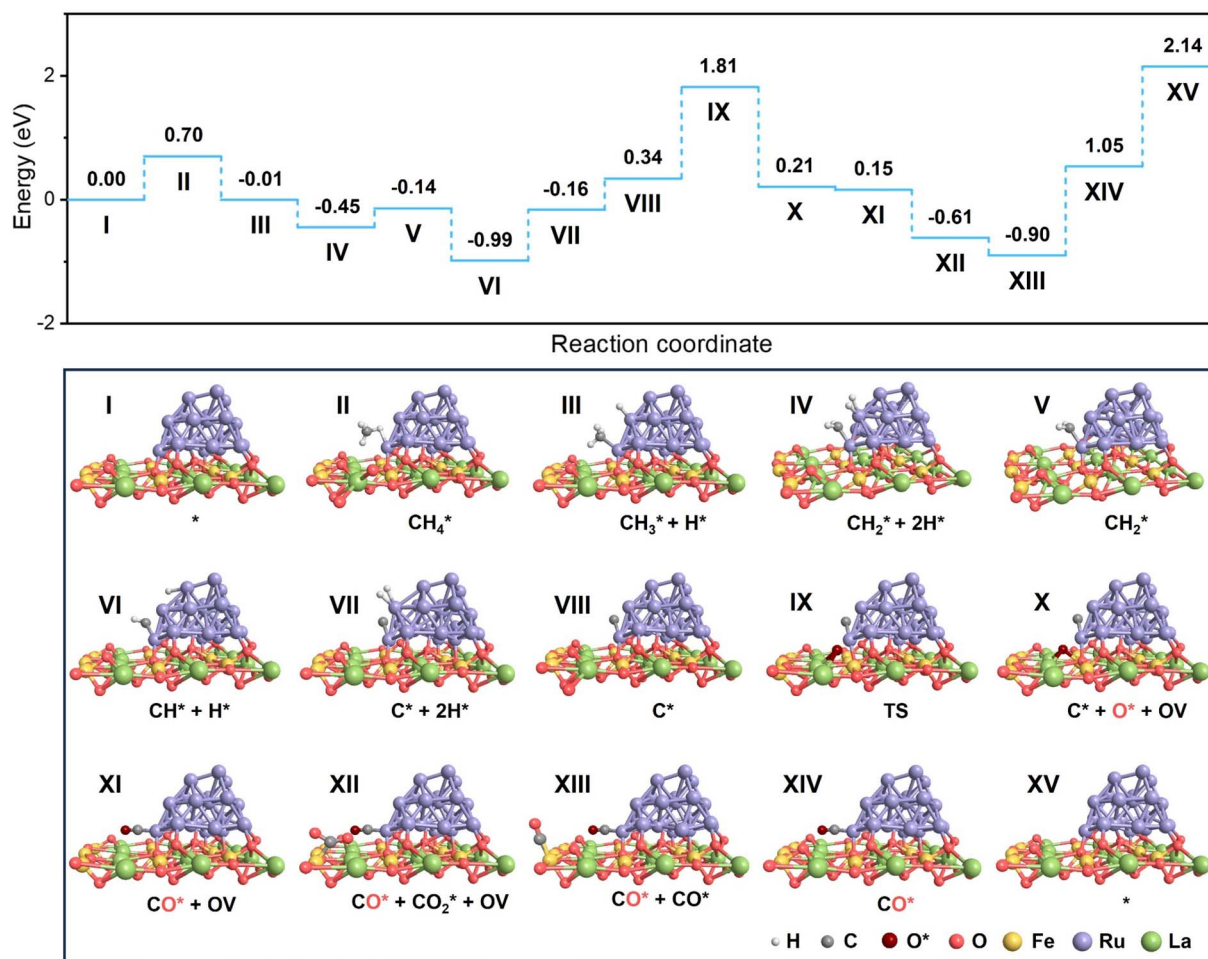
Fig. 5 Relative energy diagrams of CH_4 and CO_2 conversion on $Ru/LaFeO_3$ simulated by DFT calculation and some corresponding structures of the key reaction intermediates during the CH_4 dissociation and CO_2 conversion processes.

in activation and conversion of CH_4 and CO_2, explaining its excellent performance in light-driven DRM.

Based on both experimental findings and theoretical results, a light-driven DRM mechanism over the $Ru/LaFeO_3$ catalyst is proposed (Fig. 6). Upon light irradiation, photoexcited electrons migrate directionally to the Ru NPs, as well as the La and Fe sites, while photogenerated holes accumulated on the surface LOs (step I). Following the synergistic activation of light-induced heat and charge carriers, CH_4 molecules undergo cleavage at Ru sites and produce C* and H* species *via* sequential dehydrogenation (step II). The accumulated H* species are reduced to H_2 at the electron-rich Ru sites. Simultaneously, photoexcited electrons weaken the Fe–O or La–O bonds, promoting the migration of LOs and the generation of OVs. The migrated LOs combine with C* to form CO* (step II), while the CO_2 molecules adsorb on the OVs-rich $LaFeO_3$ surface and dissociate in the presence of photoexcited electrons into CO* and provides O to refill the OVs (step III). Finally, the adsorbed CO* desorbs from the catalyst surface as CO gas, completing the catalytic cycle (step IV).
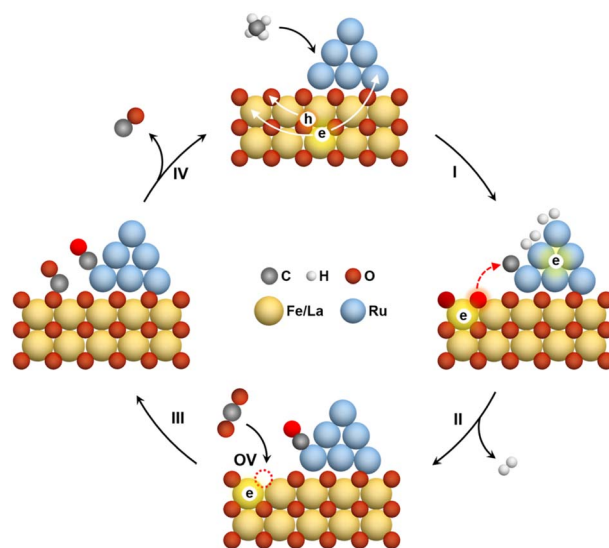

Fig. 6 Illustration of the proposed photothermal DRM mechanism over $Ru/LaFeO_3$.

Conclusions

In summary, we have developed Ru/LaFeO$_3$ as an efficient photothermal catalyst that exhibits exceptional light-driven DRM performance. This system achieves a methane TOF of 0.64 s^{-1} and a LTCEE of 16.3%. The high catalytic activity is attributed to the synergistic modulation of the catalyst's electronic structure induced by Ru loading and light excitation, in which electrons accumulate at the Ru, La, and Fe sites, and holes gather at lattice oxygens (LOs). This charge redistribution weakens the La/Fe–O bonds and promotes LO migration, enabling efficient CH$_4$ activation and oxidation at Ru sites, while *in situ* generating OVs. These OVs reduce the activation energy barrier of CO$_2$ dissociation, promoting its cleavage into CO and replenishing OVs through O* species, thereby completing the catalytic cycle. This work deciphers the feasibility of activating LOs through the dual action of cocatalysts and photoelectrons in modulating the catalyst's electronic structure, offering a strategic blueprint to fabricate high-performance catalysts toward solar-powered DRM.

Author contributions

J. Li and S. Wang conceived the project. J. Li designed and carried out all the experiments. B. Su, J. Li and X. Hao provided support with the theoretical concepts and experiment design software operation. J. Zhao assisted with theoretical calculations. J. Li prepared the initial manuscript. Z. Ding, M. Huang, M. Yang, Z. Lan and S. Wang revised the manuscript. All the authors discussed the results and provided feedback on the manuscript.

Conflicts of interest

There are no conflicts of interest to declare.

Data availability

The datasets supporting this article have been uploaded as part of the supplementary information (SI). Supplementary information is available. See DOI: https://doi.org/10.1039/d5sc05708f.

Acknowledgements

Notes and references

1 Q. Zhu, H. Zhou, L. Wang, L. Wang, C. Wang, H. Wang, W. Fang, M. He, Q. Wu and F.-S. Xiao, *Nat. Catal.*, 2022, **5**, 1030–1037.

2 X. Li, C. Wang and J. Tang, *Nat. Rev. Mater.*, 2022, **7**, 617–632.

3 Q. Hao, Z. Li, Y. Zhu, Y. Shi, M. Huo, H. Yuan, S. Ouyang and T. Zhang, *Adv. Funct. Mater.*, 2024, **34**, 2403848.

4 S. Chu and Q. Wang, *Front. Energy*, 2024, **18**, 717–726.

5 M. Zhou, H. Wang, R. Liu, Z. Liu, X. Xiao, W. Li, C. Gao, Z. Lu, Z. Jiang, W. Shi and Y. Xiong, *Angew. Chem., Int. Ed.*, 2024, **63**, e202407468.

6 J. Wang, R. Li, D. Zeng, W. Wang, Y. Zhang, L. Zhang and W. Wang, *Chem. Eng. J.*, 2023, **452**, 139505.

7 B. Su, Y. Kong, S. Wang, S. Zuo, W. Lin, Y. Fang, Y. Hou, G. Zhang, H. Zhang and X. Wang, *J. Am. Chem. Soc.*, 2023, **145**, 27415–27423.

8 X. Xu, J. Lu, B. Su, J. Chen, X. Chen and S. Wang, *Acta Phys.–Chim. Sin.*, 2025, **41**, 100153.

9 Q. Huang, J. Cai, F. Wei, Y. Fan, Z. Liang, K. Liu, X. F. Lu, Z. Ding and S. Wang, *J. Mater. Chem. A*, 2024, **12**, 21334–21340.

10 B. Su, S. Wang, W. Xing, K. Liu, S.-F. Hung, X. Chen, Y. Fang, G. Zhang, H. Zhang and X. Wang, *Angew. Chem., Int. Ed.*, 2025, **64**, e02505453.

11 H. Wang, G. Cui, H. Lu, Z. Li, L. Wang, H. Meng, J. Li, H. Yan, Y. Yang and M. Wei, *Nat. Commun.*, 2024, **15**, 3765.

12 J. Sasson Bitters, T. He, E. Nestler, S. D. Senanayake, J. G. Chen and C. Zhang, *J. Energy Chem.*, 2022, **68**, 124–142.

13 J. S. Bitters, T. N. He, E. Nestler, S. D. Senanayake, J. G. G. Chen and C. Zhang, *J. Energy Chem.*, 2022, **68**, 124–142.

14 H. Xiong, Y. Dong, C. Hu, Y. Chen, H. Liu, R. Long, T. Kong and Y. Xiong, *J. Am. Chem. Soc.*, 2024, **146**, 9465–9475.

15 Y. Yao, B. Li, X. Gao, Y. Yang, J. Yu, J. Lei, Q. Li, X. Meng, L. Chen and D. Xu, *Adv. Mater.*, 2023, **35**, e2303654.

16 Y. Tang, Y. Li, W. Bao, W. Yan, J. Zhang, Y. Huang, H. Li, Z. Wang, M. Liu and F. Yu, *Appl. Catal., B*, 2023, **338**, 123054.

17 Q. Li, H. Wang, M. Zhang, G. Li, J. Chen and H. Jia, *Angew. Chem., Int. Ed.*, 2023, **135**, e202300129.

18 Y. Yang, Z. Chai, X. Qin, Z. Zhang, A. Muhetaer, C. Wang, H. Huang, C. Yang, D. Ma, Q. Li and D. Xu, *Angew. Chem., Int. Ed.*, 2022, **61**, e202200567.

19 Z. Q. Rao, Y. H. Cao, Z. A. Huang, Z. H. Yin, W. C. Wan, M. Z. Ma, Y. X. Wu, J. B. Wang, G. D. Yang, Y. Cui, Z. M. Gong and Y. Zhou, *ACS Catal.*, 2021, **11**, 4730–4738.

20 J. Li, J. Zhao, S. Wang, K.-S. Peng, B. Su, K. Liu, S.-F. Hung, M. Huang, G. Zhang, H. Zhang and X. Wang, *J. Am. Chem. Soc.*, 2025, **147**, 14705–14714.

21 S. Shoji, X. B. Peng, A. Yamaguchi, R. Watanabe, C. Fukuhara, Y. Cho, T. Yamamoto, S. Matsumura, M. W. Yu, S. Ishii, T. Fujita, H. Abe and M. Miyauchi, *Nat. Catal.*, 2020, **3**, 148–153.

22 F. Wei, J. Zhao, Y.-C. Liu, Y.-H. Hsu, S.-F. Hung, J. Fu, K. Liu, W. Lin, Z. Yu, L. Tan, X. F. Lu, C. Feng, H. Zhang and S. Wang, *Nat. Commun.*, 2025, **16**, 6586.

23 Y. Liu, W. Xue, X. Liu, F. Wei, X. Lin, X. F. Lu, W. Lin, Y. Hou, G. Zhang and S. Wang, *Small*, 2024, **20**, 2402004.

24 S. Chen, L. Zeng, H. Tian, X. Li and J. Gong, *ACS Catal.*, 2017, **7**, 3548–3559.

25 C. He, S. Wu, Q. Li, M. Li, J. Li, L. Wang and J. Zhang, *Chem*, 2023, **9**, 3224–3244.

26 Y. Li, Z. Li, N. Wang, Y. Zha, K. Zheng, Y. Xu, B. Liu and X. Liu, *Chem Catal.*, 2025, **5**, 101189.

27 J. He, T. Wang, X. Bi, Y. Tian, C. Huang, W. Xu, Y. Hu, Z. Wang, B. Jiang, Y. Gao, Y. Zhu and X. Wang, *Nat. Commun.*, 2024, **15**, 5422.

28 Z. Shi, H. Li, L. Zhang and Y. Cao, *J. Power Sources*, 2022, **519**, 230738.

29 X. Zhang, C. Pei, X. Chang, S. Chen, R. Liu, Z.-J. Zhao, R. Mu and J. Gong, *J. Am. Chem. Soc.*, 2020, **142**, 11540–11549.

30 R. Maity, M. S. Sheikh, A. Dutta and T. P. Sinha, *J. Electron. Mater.*, 2019, **48**, 4856–4865.

31 A. G. Bhavani, W. Y. Kim and J. S. Lee, *ACS Catal.*, 2013, **3**, 1537–1544.

32 B. Yang, K. Liu, Y. Ma, J.-J. Ma, Y.-Y. Chen, M. Huang, C. Yang, Y. Hou, S.-F. Hung, J. C. Yu, J. Zhang and X. Wang, *Angew. Chem., Int. Ed.*, 2024, **63**, e202410394.

33 R. Song, G. Zhao, J. M. Restrepo-Flórez, C. J. Viasus Pérez, Z. Chen, C. Ai, A. Wang, D. Jing, A. A. Tountas, J. Guo, C. Mao, C. Li, J. Shen, G. Cai, C. Qiu, J. Ye, Y. Fu, C. T. Maravelias, L. Wang, J. Sun, Y.-F. Xu, Z. Li, J. Y. Y. Loh, N. T. Nguyen, L. He, X. Zhang and G. A. Ozin, *Nat. Energy*, 2024, **9**, 750–760.

34 A. Shahnazi and S. Firoozi, *J. CO₂ Util.*, 2021, **45**, 101455.

35 Q. Lin, J. Zhao, P. Zhang, S. Wang, Y. Wang, Z. Zhang, N. Wen, Z. Ding, R. Yuan, X. Wang and J. Long, *Carbon Energy*, 2024, **6**, e435.

36 Y. Cao, R. Guo, M. Ma, Z. Huang and Y. Zhou, *Acta Phys.–Chim. Sin.*, 2024, **40**, 2303029.

37 L. Zhou, J. M. P. Martirez, J. Finzel, C. Zhang, D. F. Swearer, S. Tian, H. Robatjazi, M. Lou, L. Dong, L. Henderson, P. Christopher, E. A. Carter, P. Nordlander and N. J. Halas, *Nat. Energy*, 2020, **5**, 61–70.

38 J. Zhang, K. Xie, Y. Jiang, M. Li, X. Tan, Y. Yang, X. Zhao, L. Wang, Y. Wang, X. Wang, Y. Zhu, H. Chen, M. Wu, H. Sun and S. Wang, *ACS Catal.*, 2023, **13**, 10855–10865.

39 J. Zhang, Y. Li, J. Sun, H. Chen, Y. Zhu, X. Zhao, L.-C. Zhang, S. Wang, H. Zhang, X. Duan, L. Shi, S. Zhang, P. Zhang, G. Shao, M. Wu, S. Wang and H. Sun, *Appl. Catal., B*, 2022, **309**, 121263.

40 H. Liu, X. Meng, T. D. Dao, H. Zhang, P. Li, K. Chang, T. Wang, M. Li, T. Nagao and J. Ye, *Angew. Chem., Int. Ed.*, 2015, **54**, 11545–11549.

41 Y. Wang, Y. Liu, L. Tan, X. Lin, Y. Fang, X. F. Lu, Y. Hou, G. Zhang and S. Wang, *J. Mater. Chem. A*, 2023, **11**, 26804–26811.

42 B. Su, M. Zheng, W. Lin, X. F. Lu, D. Luan, S. Wang and X. W. Lou, *Adv. Energy Mater.*, 2023, **13**, 2203290.

43 J. Cai, X. Li, B. Su, B. Guo, X. Lin, W. Xing, X. F. Lu and S. Wang, *J. Mater. Sci. Technol.*, 2025, **234**, 82–89.

44 C. Zhang, X. Tao, W. Jiang, J. Guo, P. Zhang, C. Li and R. Li, *Acta Phys.–Chim. Sin.*, 2024, **40**, 2303034.

45 E. Lu, J. Tao, C. Yang, Y. Hou, J. Zhang, X. Wang and X. Fu, *Acta Phys.–Chim. Sin.*, 2023, **39**, 2211029.

46 B. Li, W. Wang, J. Zhao, Z. Wang, B. Su, Y. Hou, Z. Ding, W. J. Ong and S. Wang, *J. Mater. Chem. A*, 2021, **9**, 10270–10276.

47 M. Liu, G. Zhang, X. Liang, Z. Pan, D. Zheng, S. Wang, Z. Yu, Y. Hou and X. Wang, *Angew. Chem., Int. Ed.*, 2023, **62**, e202304694.

48 X. Xu, C. Shao, J. Zhang, Z. Wang and K. Dai, *Acta Phys.–Chim. Sin.*, 2024, **40**, 2309031.

49 J. Su, J. Zhang, S. Chai, Y. Wang, S. Wang and Y. Fang, *Acta Phys.–Chim. Sin.*, 2024, **40**, 2408012.

50 F. Liu, J. Deng, B. Su, K.-S. Peng, K. Liu, X. Lin, S.-F. Hung, X. Chen, X. F. Lu, Y. Fang, G. Zhang and S. Wang, *ACS Catal.*, 2025, **15**, 1018–1026.

51 Y. Zou, H. Chen, Y. Hou, W. Xing, Z. Pan, O. Savateev, M. Anpo and G. Zhang, *Adv. Funct. Mater.*, 2025, e16479.

52 L. Huang, B. Li, B. Su, Z. Xiong, C. Zhang, Y. Hou, Z. Ding and S. Wang, *J. Mater. Chem. A*, 2020, **8**, 7177–7183.

53 C. Guo, Y. Cui, W. Zhang, X. Du, X. Peng, Y. Yu, J. Li, Y. Wu, Y. Huang, T. Kong and Y. Xiong, *Adv. Mater.*, 2025, **37**, 2500928.

54 Y.-F. Wang, M.-Y. Qi, M. Conte, Z.-R. Tang and Y.-J. Xu, *Angew. Chem., Int. Ed.*, 2024, **63**, e202407791.

55 W. Zhang, C. Fu, J. Low, D. Duan, J. Ma, W. Jiang, Y. Chen, H. Liu, Z. Qi, R. Long, Y. Yao, X. Li, H. Zhang, Z. Liu, J. Yang, Z. Zou and Y. Xiong, *Nat. Commun.*, 2022, **13**, 2806.

56 W. Jiang, J. Low, K. Mao, D. Duan, S. Chen, W. Liu, C.-W. Pao, J. Ma, S. Sang, C. Shu, X. Zhan, Z. Qi, H. Zhang, Z. Liu, X. Wu, R. Long, L. Song and Y. Xiong, *J. Am. Chem. Soc.*, 2021, **143**, 269–278.

57 W. Zhou, B. H. Wang, L. Tang, L. Chen, J. K. Guo, J. B. Pan, B. Lei, B. Hu, Z. J. Bai, M. Tulu, Z. X. Li, X. Wang, C. T. Au and S. F. Yin, *Adv. Funct. Mater.*, 2023, **33**, 2214068.

58 S. Luo, H. Song, F. Ichihara, M. Oshikiri, W. Lu, D.-M. Tang, S. Li, Y. Li, Y. Li, P. Davin, T. Kako, H. Lin and J. Ye, *J. Am. Chem. Soc.*, 2023, **145**, 20530–20538.

59 S. Singh, R. Verma, N. Kaul, J. Sa, A. Punjal, S. Prabhu and V. Polshettiwar, *Nat. Commun.*, 2023, **14**, 2551.

60 Q. Cheng, X. Yao, L. Ou, Z. Hu, L. Zheng, G. Li, N. Morlanes, J. L. Cerrillo, P. Castaño, X. Li, J. Gascon and Y. Han, *J. Am. Chem. Soc.*, 2023, **145**, 25109–25119.